

Predictions of microstructure and stress in two-dimensional pure shearing of a dense viscous suspension

James T. Jenkins¹ †, Ryohei Seto² and Luigi La Ragione³

¹School of Civil and Environmental Engineering, Cornell University, Ithaca, NY 14853, USA

²Wenzhou Institute, University of Chinese Academy of Sciences, Wenzhou, Zhejiang 325000, China

³Dipartimento di Scienze dell'Ingegneria Civile e dell'Architettura, Politecnico di Bari, 70125 Bari, Italy

(Received ?; revised ?; accepted ?. - To be entered by editorial office)

We consider pure shearing of a dense layer of spheres in a viscous fluid and employ force and moment equilibrium to determine the trajectory of particle pairs that contribute to the stress. In doing this, we use Stokesian Dynamics simulations to guide the choice of the near-contacting pairs that follow such a trajectory. We specify the boundary conditions on the representative trajectory, determine the distribution of particles along it, and how the stress depends on the microstructure and strain-rate. We test the resulting predictions using the numerical simulations. Also, we show that the relation between the tensors of stress and strain rate involves the second and fourth moments of the particle distribution function.

Key words: Authors should not enter keywords on the manuscript, as these must be chosen by the author during the online submission process and will then be added during the typesetting process (see <http://journals.cambridge.org/data/relatedlink/jfm-keywords.pdf> for the full list)

1. Introduction

In a recent study, Jenkins and La Ragione (2015) determine the typical trajectory of an equilibrated pair of particles of a dense, two-dimensional suspensions of spheres subjected to a simple shearing flow. They evaluate the distribution function of near-contacting neighbors along the trajectory and, using this distribution function and the expression for the force between two equilibrated near-contacting neighbors, they predict the particle pressure, the difference in normal stresses, and the difference between the average rotation of the spheres and half the vorticity of the average velocity.

Here, we focus on *pure shearing* (also called planar extensional flow) of a dense layer of spheres and, as an extension of the previous work, also introduce moment equilibrium. We employ Stokesian Dynamics numerical simulations to guide the choice of the near-contacting pairs on a representative trajectory that contributes most to the inter-particle stress. We specify the boundary conditions on the representative trajectory, determine the distribution of particles along it, and the relationship between stress, microstructure and strain-rate. We test these predictions against the results of the numerical simulations.

† Email address for correspondence: jtj2@cornell.edu

We show that the relation between the stress and strain rate tensors involves the second and fourth moments of the particle distribution, and place this and other aspects of our approach in the context of earlier models that focused on the second moment (Phan-Thien 1995; Stickel, et al. 2006; Goddard, 2006).

The approximate satisfaction of force and moment equilibrium of particles in the flow plays an important role in what we do. In that regard, we operate in the spirit of Nazockdast and Morris (2012a, 2012b, 2013) or that of the statistical characterization by Thomas et. al. (2018) of equilibrated particles sheared in two dimensions, but in the limit of dense flows of the simpler pure shearing flow. The analysis must be extended to three-dimensional rotational shearing flows before it can be placed in relation to phenomenological relations that have resulted from experiments on dense three-dimensional shearing flows (Boyer, et al. 2011; Guazzelli and Pouliquen 2018).

2. Micro-mechanics

A steady, planar, pure shearing flow of a dense suspensions of identical spheres with radius a is characterized by an average rate of deformation tensor \mathbf{D} with nonzero components $D_{11} = -D_{22} = \dot{\gamma}$, where x_1 and x_2 are the axes in the directions of greatest extension and compression, respectively, and $\dot{\gamma}$ is the constant shear rate. We focus on a typical pair of spheres and their near-contacting neighbors, and take $\hat{\mathbf{d}}^{(BA)}$ to be the unit vector directed from the center of sphere A to that of sphere B , with $\hat{\mathbf{d}}^{(AB)} = -\hat{\mathbf{d}}^{(BA)}$ (see Fig. 1). Then, with $\theta^{(BA)}$ the time-dependent angle between $\hat{\mathbf{d}}^{(BA)}$ and the x_2 axis,

$$\hat{d}_\alpha^{(BA)} = (\sin \theta^{(BA)}, \cos \theta^{(BA)}) \quad (2.1)$$

and the components of the unit tangent vector, $\hat{\mathbf{t}}^{(BA)} = -\hat{\mathbf{t}}^{(AB)}$, perpendicular to it, are

$$t_\alpha^{(BA)} = (\cos \theta^{(BA)}, -\sin \theta^{(BA)}), \quad (2.2)$$

or $t_\alpha^{(BA)} = \varepsilon_{\alpha\beta} \hat{d}_\beta^{(BA)}$, where $\varepsilon_{12} = -\varepsilon_{21} = 1$ and $\varepsilon_{11} = \varepsilon_{22} = 0$.

2.1. Kinematics

In a pure shearing flow, the relative motion of the center of particle B with respect to the center of particle A is

$$v_\alpha^{(BA)} = \frac{ds^{(BA)}}{dt} \hat{d}_\alpha^{(BA)} + 2a \frac{d\theta^{(BA)}}{dt} \hat{t}_\alpha^{(BA)}, \quad (2.3)$$

where s is the separation of the edges along the line of centers. The relative velocity of their points of near contact is, then,

$$v_\alpha^{(BA)} + a(\omega^{(A)} + \omega^{(B)}) \hat{t}_\alpha^{(BA)} \equiv v_\alpha^{(BA)} + aS \hat{t}_\alpha^{(BA)}, \quad (2.4)$$

where ω is the angular velocity of the sphere and S is their sum.

The interaction of A with a near contacting neighbors n , other than B , is treated differently; the sphere n is assumed to move relative to A with the average flow. Then, neglecting fluctuations in translational velocity, the relative velocity of centers of pair nA is

$$v_\alpha^{(nA)} = 2a D_{\alpha\beta} \hat{d}_\beta^{(nA)} \quad (2.5)$$

and the relative velocity of the points of near contact nA is

$$v_\alpha^{(nA)} + a\omega^{(A)} \hat{t}_\alpha^{(nA)}. \quad (2.6)$$

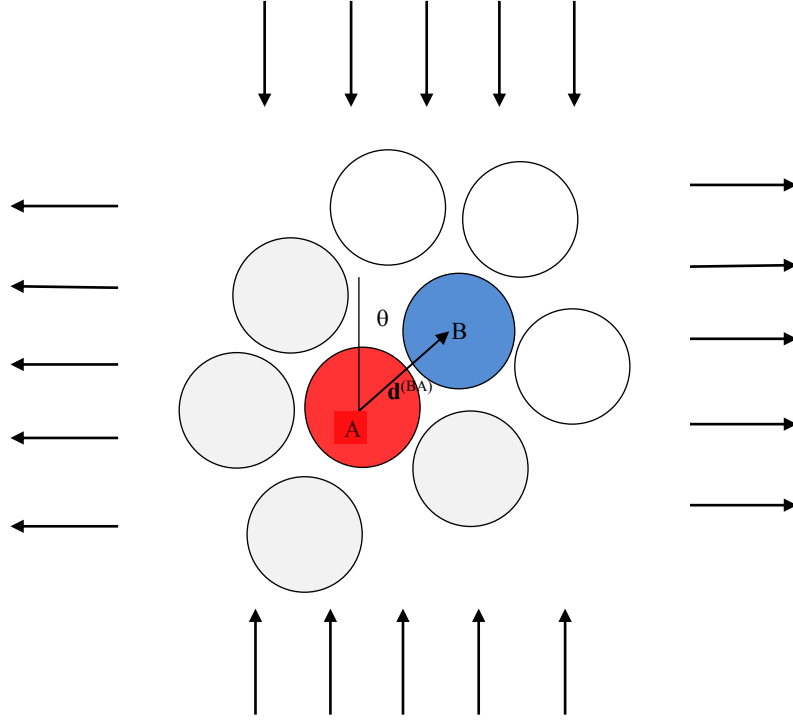


Figure 1: The pair AB and the near-contacting neighbors of A , showing the angle $\theta^{(BA)}$ and the vector $\mathbf{d}^{(BA)}$ from the center of A to that of B .

2.2. Force

The force of interaction between a typical pair AB of particles is related to the relative velocity and distance between their points of near contact. According to Jeffrey and Onishi (1984) and Jeffrey (1992), the force $\mathbf{F}^{(BA)}$ exerted by sphere B on sphere A through a fluid with viscosity μ , is

$$F_{\alpha}^{(BA)} = 6\pi\mu a K_{\alpha\beta}^{(BA)} v_{\beta}^{(BA)} - \frac{F_0}{s^{(BA)}} \hat{d}_{\alpha}^{(BA)} - 9.54\pi\mu a^2 \left(\hat{t}_{\beta} D_{\beta\xi} \hat{d}_{\xi} \right) \hat{t}_{\alpha}^{(BA)} + \pi\mu a^2 \left[\ln \left(\frac{a}{s^{(BA)}} \right) - 0.96 \right] \omega^{(A)} \hat{t}_{\alpha}^{(BA)} + \pi\mu a^2 \ln \left(\frac{a}{s^{(BA)}} \right) \omega^{(B)} \hat{t}_{\alpha}^{(BA)}, \quad (2.7)$$

where

$$K_{\alpha\beta}^{(BA)} = \frac{1}{4} \frac{a}{s^{(BA)}} \hat{d}_{\alpha}^{(BA)} \hat{d}_{\beta}^{(BA)} + \left[\frac{1}{6} \ln \left(\frac{a}{s^{(BA)}} \right) + 0.64 \right] \hat{t}_a^{(BA)} \hat{t}_{\beta}^{(BA)} \quad (2.8)$$

and the constant terms have been retained because they are the same order as the logarithms. The interaction force also includes a short-range repulsive force of strength F_0 (e.g. Singh and Nott, 2000).

We take the near-contacting neighbors, $n \neq B$, to be those that most influence equilibrium and make the greatest contribution to the stress. There are $k - 1$ of these per sphere and we assume that the separation between their edges is \bar{s} . The number, k , of near-contacting neighbors is expected to be less, perhaps far less, than the number of nearest neighbors and to depend upon the area fraction ν .

For the near-contacting neighbors, the corresponding force is based on the average motion and the separation \bar{s} :

$$\begin{aligned} F_\alpha^{(nA)} = & \frac{3}{\bar{s}} a^2 \pi \mu \left(D_{\beta\xi} \hat{d}_\xi^{(nA)} \hat{d}_\beta^{(nA)} \right) \hat{d}_\alpha^{(nA)} + \pi \mu a^2 \left[\ln \left(\frac{a}{\bar{s}} \right) - 0.96 \right] \omega^{(A)} \hat{t}_\alpha^{(nA)} \\ & + 2a^2 \pi \mu \left[\ln \left(\frac{a}{\bar{s}} \right) - 0.96 \right] \left(D_{\beta\xi} \hat{t}_\xi^{(nA)} \hat{d}_\beta^{(nA)} \right) \hat{t}_\alpha^{(nA)} - \frac{F_0}{\bar{s}} \hat{d}_\alpha^{(nA)}. \end{aligned} \quad (2.9)$$

2.3. Equilibrium

As do Jenkins and La Ragione (2015), we require the equilibrium of a typical pair of spheres under the action of their near-contacting neighbors. However, while they employ only force equilibrium, here we consider the equilibrium of both force and moment. The focus on a flow in which there is no average rotation makes this easier to do; and the possibility of solving for both the translational and rotational degrees of freedom of a typical pair should increase the accuracy of the modeling.

Force equilibrium for particle A is

$$F_\alpha^{(BA)} + \sum_{n \neq B}^{N^{(A)}} F_\alpha^{(nA)} = 0; \quad (2.10)$$

and that for particle B is

$$F_\alpha^{(AB)} + \sum_{m \neq A}^{N^{(B)}} F_\alpha^{(mB)} = 0, \quad (2.11)$$

with $F_\alpha^{(BA)} = -F_\alpha^{(AB)}$. The difference in the force balances projected along $\hat{\mathbf{d}}^{(BA)}$ is

$$3\pi\mu a \frac{a}{s^{(BA)}} \frac{ds^{(BA)}}{dt} - 2 \frac{F_0}{s^{(BA)}} + 6\pi\mu a^2 \frac{a}{\bar{s}} \hat{d}_\alpha^{(BA)} J_{\alpha\beta\gamma} D_{\beta\gamma} - 2 \frac{F_0}{\bar{s}} Y_\alpha \hat{d}_\alpha^{(BA)} = 0; \quad (2.12)$$

while along $\hat{t}_\alpha^{(BA)}$ is

$$\begin{aligned} 0 = & 4 \left[\ln \left(\frac{a}{s^{(BA)}} \right) + 3.84 \right] \frac{d\theta^{(BA)}}{dt} - 19 \hat{t}_\beta^{(BA)} D_{\beta\xi} \hat{d}_\xi^{(BA)} \\ & + \left[2 \ln \left(\frac{a}{s^{(BA)}} \right) - 0.96 \right] S + \left[\ln \left(\frac{a}{\bar{s}} \right) - 0.96 \right] S \varepsilon_{\alpha\beta} Y_\beta^{(BA)} t_\alpha^{(BA)} \\ & + 6 \frac{a}{\bar{s}} D_{\beta\xi} J_{\alpha\xi\beta} t_\alpha^{(BA)} + 2 \left[2 \ln \left(\frac{a}{\bar{s}} \right) - 1.92 \right] D_{\beta\xi} J_{\alpha\xi\beta}^{(BA)} t_\alpha^{(BA)}, \end{aligned} \quad (2.13)$$

with

$$J_{\alpha\xi\beta}^{(BA)} = \sum_{n \neq B}^{N^{(A)}} \hat{d}_\alpha^{(nA)} \hat{d}_\beta^{(nA)} \hat{d}_\xi^{(nA)} \quad (2.14)$$

Microstructure and stress in two-dimensional pure shearing of dense viscous suspension **5**
and

$$Y_{\alpha}^{(BA)} = \sum_{n \neq B}^{N^{(A)}} \hat{d}_{\alpha}^{(nA)}. \quad (2.15)$$

In writing Eqs.(2.12) and (2.13), we assume that $J_{\alpha\xi\beta}^{(BA)} = -J_{\alpha\xi\beta}^{(AB)}$ and $Y_{\alpha}^{(BA)} = -Y_{\alpha}^{(AB)}$; that is, the arrangement of near-contacting neighbors of B is the reflection of that of A. The terms proportional to S incorporate the influence of the rotations on force equilibrium.

Moment equilibrium for particle A is

$$\varepsilon_{\alpha\beta} d_{\alpha}^{(BA)} F_{\beta}^{(BA)} + \varepsilon_{\alpha\beta} \sum_{n \neq B}^{N^{(A)}} d_{\alpha}^{(nA)} F_{\beta}^{(nA)} = 0, \quad (2.16)$$

and that for particle B is

$$\varepsilon_{\alpha\beta} d_{\alpha}^{(AB)} F_{\beta}^{(AB)} + \varepsilon_{\alpha\beta} \sum_{m \neq A}^{N^{(B)}} d_{\alpha}^{(mB)} F_{\beta}^{(mB)} = 0; \quad (2.17)$$

so their sum is

$$\begin{aligned} 0 = & 4 \left[\ln \left(\frac{a}{s^{(BA)}} \right) + 3.84 \right] \frac{d\theta^{(BA)}}{dt} - 19 \hat{t}_{\mu}^{(BA)} D_{\mu\xi} \hat{d}_{\xi}^{(BA)} \\ & + \left[2 \ln \left(\frac{a}{s^{(BA)}} \right) - 0.96 \right] S + \left[\ln \left(\frac{a}{s} \right) - 0.96 \right] S (k-1) \\ & + 2 \left[2 \ln \left(\frac{a}{s} \right) - 1.92 \right] \varepsilon_{\xi\nu} A_{\nu\mu}^{(BA)} D_{\mu\xi}, \end{aligned} \quad (2.18)$$

with

$$A_{\nu\mu}^{(BA)} = \sum_{n \neq B}^{N^{(A)}} \hat{d}_{\nu}^{(nA)} \hat{d}_{\mu}^{(nA)} \quad (2.19)$$

and, again, $A_{\nu\mu}^{(BA)} = A_{\nu\mu}^{(AB)}$.

The tensors \mathbf{A} , \mathbf{J} and \mathbf{Y} provide information on the distribution of spheres about a typical pair A - B . We assume here that the distributions about a pair at a given orientation is the average over all pairs at that orientation. These average distributions should depend on both $\hat{\mathbf{d}}^{(AB)}$ and \mathbf{D} . As do Jenkins and La Ragione (2015), we treat the local equilibrium with the approximation that \mathbf{A} , \mathbf{J} and \mathbf{Y} are independent of \mathbf{D} . Then,

$$A_{\nu\mu}^{(BA)} = b_1 \delta_{\nu\mu} + b_2 \hat{d}_{\mu}^{(BA)} \hat{d}_{\nu}^{(BA)}, \quad (2.20)$$

$$J_{\alpha\xi\beta}^{(BA)} = b_3 \hat{d}_{\alpha}^{(BA)} \hat{d}_{\xi}^{(BA)} \hat{d}_{\beta}^{(BA)} + b_4 \left(\hat{d}_{\alpha}^{(BA)} \delta_{\xi\beta} + \hat{d}_{\xi}^{(BA)} \delta_{\alpha\beta} + \hat{d}_{\beta}^{(BA)} \delta_{\xi\alpha} \right), \quad (2.21)$$

and

$$Y_{\alpha}^{(BA)} = b_5 \hat{d}_{\alpha}^{(BA)} \quad (2.22)$$

To calculate the coefficients, Jenkins and La Ragione (2015) assume that given sphere B , the remaining near-contacting neighbors of A spheres are distributed uniformly around its circumference. The results are given as a function of coordination number k through

$$b = -\frac{3\sqrt{3}(k-1)}{16\pi}, \quad (2.23)$$

by

$$b_1 = \frac{k-1}{2} - b, \quad b_2 = 2b, \quad b_3 = 0, \text{ and } b_4 = b, \quad b_5 = 4b. \quad (2.24)$$

In the pure shearing flow of interest,

$$\hat{t}_\mu^{(BA)} D_{\mu\xi} \hat{d}_\xi^{(BA)} = \dot{\gamma} \sin 2\theta \quad \text{and} \quad \hat{d}_\mu^{(BA)} D_{\mu\xi} \hat{d}_\xi^{(BA)} = -\dot{\gamma} \cos 2\theta. \quad (2.25)$$

We use these in the differences of the components of the force balances, make lengths dimensionless by the sphere radius a , time by the inverse of the shear rate, forces by $\pi a^3 \mu \dot{\gamma}$, write the dimensionless repulsive force as $\hat{F} = F_0/(\pi a^3 \mu \dot{\gamma})$, and remove the superscript (BA) . Then, the normal component becomes

$$\frac{1}{s} \frac{ds}{d\gamma} = \frac{2}{3} \hat{F} \left(\frac{1}{s} + \frac{4b}{\bar{s}} \right) + \frac{4b}{\bar{s}} \cos 2\theta; \quad (2.26)$$

and the tangential component is

$$\left[\ln \left(\frac{1}{s} \right) + 3.84 \right] \frac{d\theta}{d\gamma} = \left[c_1 + c_2 \ln \left(\frac{1}{s} \right) \right] \sin 2\theta, \quad (2.27)$$

with

$$c_1 = 4.77 - 3 \frac{b}{\bar{s}} \quad \text{and} \quad c_2 = \frac{6b}{(4b - k + 1)} \frac{1/\bar{s}}{\ln(1/\bar{s}) - 0.96}. \quad (2.28)$$

and we have employed the difference in force balance and the sum of moment equilibrium to write

$$S = -2c_2 \sin 2\theta. \quad (2.29)$$

The balances of force and moment, Eqs.(2.26), (2.27), and (2.29), employed in Eq. (2.7), provide an expression for $\mathbf{F}^{(BA)}$ in terms of average quantities:

$$\begin{aligned} F_\alpha^{(BA)} = & 4b \frac{F_0}{\bar{s}} \hat{d}_\alpha^{(BA)} + \pi \mu a^3 \frac{6b}{\bar{s}} \cos 2\theta \dot{\gamma} \hat{d}_\alpha^{(BA)} + \pi \mu a^2 (2c_1 + 0.96c_2) \sin 2\theta \dot{\gamma} \hat{t}_\alpha^{(BA)} \\ & - 9.54 \pi \mu a^2 \sin 2\theta \dot{\gamma} \hat{t}_\alpha^{(BA)}. \end{aligned} \quad (2.30)$$

This is later used in the calculation of the stress

2.4. Representative trajectory

We identify the representative trajectory as that which particle B traverses with respect to particle A in a succession of equilibrated states. The other near-contacting particles, n , of the pair are assumed to move with the average flow, at the constant distance \bar{s} from the pair. The equation that determines this trajectory results from force and moment equilibrium and is a function of two parameters: the average number of near-contacting particles, k , and the distance, \bar{s} . Upon combining Eqs. (2.26) and (2.27), it is

$$\frac{ds}{d\theta} = \frac{2}{3\bar{s}} \frac{\hat{F}(\bar{s} + 4bs) + 6bs \cos 2\theta}{[c_1 + c_2 \ln(1/s)] \sin 2\theta} \left[\ln \left(\frac{1}{s} \right) + 3.84 \right]. \quad (2.31)$$

Within the θ interval 0 to $\pi/2$, the trajectory begins at θ_0 and ends at θ_1 , and both angles must be determined. Because of the presence of \hat{F} , the trajectory is asymmetric about $\pi/4$, and θ_0 differs from $\pi/2 - \theta_1$.

The amount of total strain, $\hat{\gamma}$, necessary to complete the trajectory may be calculated from the pair interaction in the average flow. From Eq. (2.27)

$$\frac{d\gamma}{d\theta} = \frac{\ln(1/s) + 3.84}{[c_1 + c_2 \ln(1/s)] \sin 2\theta}; \quad (2.32)$$

so,

$$\hat{\gamma} = \int_{\theta_0}^{\theta_1} \frac{\ln(1/s) + 3.84}{[c_1 + c_2 \ln(1/s)] \sin 2\theta} d\theta. \quad (2.33)$$

2.5. Particle distribution

We next introduce the distribution of near-contacting neighbors along the trajectory, $A(\theta)$, defined so that $A(\theta) d\theta$ is the average number of such particles within the element $d\theta$. At steady state, the flux, $A(\theta) d\theta/d\gamma$, of these equilibrated particles along the trajectory is constant. That is, particles are more likely to be where the velocity along the trajectory is least. Because the repulsive force breaks the symmetry of approach and departure, the distribution is anticipated to be asymmetric about $\pi/4$. In computations, we implement the flux condition as a differential equation

$$\frac{dA}{d\theta} = -\frac{A}{\dot{\theta}} \frac{d\dot{\theta}}{d\theta}, \quad (2.34)$$

with

$$\frac{d\dot{\theta}}{d\theta} = \frac{\partial \dot{\theta}}{\partial \theta} + \frac{\partial \dot{\theta}}{\partial s} \frac{ds}{d\theta}. \quad (2.35)$$

The distribution $A(\theta)$ is related to the average number near-contacting neighbors per particle by

$$4 \int_{\theta_0}^{\theta_1} A(\theta) d\theta = k. \quad (2.36)$$

We implement this as a differential equation for the partial number of near-contacting neighbors

$$I(\theta) \equiv \int_{\theta_0}^{\theta} A(\theta') d\theta', \quad (2.37)$$

as

$$\frac{dI}{d\theta} = A(\theta), \quad (2.38)$$

with boundary conditions $I(\theta_0) = 0$ and $I(\theta_1) = k/4$.

Given that the beginning and ending angles of the trajectory differ, we take the beginning and ending values of the particle separation to be the same. There are three first-order differential equations, Eqs. (2.31), (2.34), and (2.38), for s , A , and I as functions of θ , and four boundary conditions: one for each of s_0 and s_1 that introduce a single parameter, and two for I . Consequently, θ_1 may be determined as part of the solution. The inputs are θ_0 , $s_0 = s_1$, \bar{s} , and k . In Appendix B, we provide the Matlab code that is employed in the solver. We generate solutions and compare them with the results of Stokesian Dynamics simulations in a later section.

3. Particle stress

Knowledge of the distribution of near-contacting neighbors $A(\theta)$ and the contact forces along the trajectory permits the calculation of the macroscopic particle stress in the suspension. The stress tensor is, according to Cauchy (Love 1944, Appendix, Note B),

$$T_{\alpha\beta} = na \int_0^{2\pi} A(\theta) F_{\alpha} \hat{d}_{\beta} d\theta, \quad (3.1)$$

with F_α given by its equilibrium expression, Eq. (2.30). The dimensionless form of this, $t_{a\beta} = T_{\alpha\beta}/(2a\mu\dot{\gamma})$ with $n = \nu/(\pi a^2)$, is

$$t_{a\beta} = \nu \frac{b}{\bar{s}} \int_0^{2\pi} A(\theta) \left(2\hat{F} + 3 \cos 2\theta \right) \hat{d}_\alpha \hat{d}_\beta d\theta \\ + \nu (c_1 + 0.48c_2 - 4.77) \int_0^{2\pi} A(\theta) \sin 2\theta \hat{t}_a \hat{d}_\beta d\theta. \quad (3.2)$$

The particle shear stress,

$$\tau \equiv \frac{1}{2} (t_{11} - t_{22}), \quad (3.3)$$

is

$$\tau = -2\nu \frac{b}{\bar{s}} \int_0^{\pi/2} A(\theta) \left(2\hat{F} + 3 \cos 2\theta \right) \cos 2\theta d\theta \\ + \nu (2c_1 + 0.96c_2 - 9.54) \int_0^{\pi/2} A(\theta) \sin^2 2\theta d\theta, \quad (3.4)$$

where b , c_1 and c_2 are given in terms of k in Eqs. (2.24) and (2.28), respectively. The shear stress depends on the separation, \bar{s} , of near-contacting neighbors other than B , and on the area fraction, explicitly and through the coordination number, k . Because the direct contribution of the repulsive force to the integral is very small and the trigonometric factors associated with the other contributions are even about $\pi/4$, the shear stress is independent of the asymmetry of the particle distribution about $\pi/4$. In contrast, this asymmetry is crucial to the determination of the particle pressure.

The particle pressure,

$$p \equiv -\frac{1}{2} (t_{11} + t_{22}), \quad (3.5)$$

is

$$p = -2\nu \frac{b}{\bar{s}} \int_0^{\pi/2} A(\theta) \left(2\hat{F} + 3 \cos 2\theta \right) d\theta. \quad (3.6)$$

This pressure also depends on \bar{s} and ν and its existence is due to the asymmetry of A about $\pi/4$. This asymmetry is due to that of the separation along the representative trajectory created by \hat{F} and the influence of the asymmetry of the separation on the angular velocity, $\dot{\theta}$. The particle pressure and the mechanisms responsible for it are a focus of this paper; a particle shear stress may be calculated based on the average flow, although that determined here is several times less than this because of the approximate satisfaction of equilibrium.

Particle stresses associated with motion along the representative trajectories are compared with those measured in Stokesian Dynamics simulations after a discussion of the simulations.

4. Stokesian Dynamics

We determine the trajectories of spherical particles in the flows by performing simulation with the same conditions as the theory (a monolayer with no inertia). We impose a fixed flow profile of pure shear with shear rate $\dot{\gamma}$, †

$$\mathbf{u}^\infty(\mathbf{r}) = \mathbf{D} \cdot \mathbf{r}, \quad \mathbf{D} = \begin{pmatrix} \dot{\gamma} & 0 \\ 0 & -\dot{\gamma} \end{pmatrix}. \quad (4.1)$$

† Note: This is equivalent to the extensional rate $\dot{\epsilon}$ in Seto et al., 2017.

A simulation box with periodic boundary conditions constantly deforms according to this. Significant deformations of the simulation box can be avoided by using the Kraynik–Reinelt periodic boundary conditions, which take the deformed box to the original square box after a constant strain interval (Kraynik and Reinelt 1992, Todd and Daivis, 1998, Seto et al., 2017). Thus, the flow can be maintained for a sufficiently long time to evaluate its steady states.

Due to the negligible inertia of the particles, translational and angular velocities can be determined by solving the force and torque balance equations for the respective particles ($i = 1, \dots, N$):

$$\begin{pmatrix} \mathbf{0} \\ \mathbf{0} \end{pmatrix} = \begin{pmatrix} \mathbf{F}_H \\ \mathbf{T}_H \end{pmatrix} + \begin{pmatrix} \mathbf{F}_R \\ \mathbf{0} \end{pmatrix}. \quad (4.2)$$

Here, a vector, such as \mathbf{F}_H , represent all N particles, $\mathbf{F}_H \equiv (\mathbf{F}_H^{(1)}, \dots, \mathbf{F}_H^{(N)})$.

The hydrodynamic interactions in the Stokes, zero Reynolds number, regime are linear in the velocities:

$$\begin{pmatrix} \mathbf{F}_H \\ \mathbf{T}_H \end{pmatrix} = -\mathbf{R}_{FU} \cdot \begin{pmatrix} \mathbf{U} - \mathbf{u}^\infty \\ \boldsymbol{\Omega} \end{pmatrix} + \mathbf{R}_{FE} : \mathbf{D}_N, \quad (4.3)$$

where \mathbf{D}_N is block diagonal of N copies of \mathbf{D} . There exist several levels of approximations to construct the resistance matrices \mathbf{R}_{FU} and \mathbf{R}_{FD} . Brady and Bossis (1988) constructed them using truncated multipole expansions for the far-field interactions and a pair-wise solution for lubrication interactions. In this work, we focus on a special situation in which repulsive forces are very weak in comparison with viscous drag forces. Under such conditions, particles tend to approach their neighbors very closely. Because the resistance coefficients diverge at contacts ($s = 0$), the nearly touching hydrodynamic interactions dominate the dynamics. This is why we construct the approximate resistance matrices with the leading $1/s$ term in the normal component and the logarithmic term $\log(1/s)$ and following constants in the tangential component, using the solution for two nearly-touching rigid spheres (Jeffrey and Onishi, 1984, Jeffrey, 1992). (A detailed descriptions can be seen elsewhere, c.f. Mari et al., 2014.) The hydrodynamic interaction is effective until a cutoff distance, $s < 0.10$; thus, the resistance coefficients remain positive in this range. The repulsive force employed in this work is the same as that used in Nott and Brady (1994):

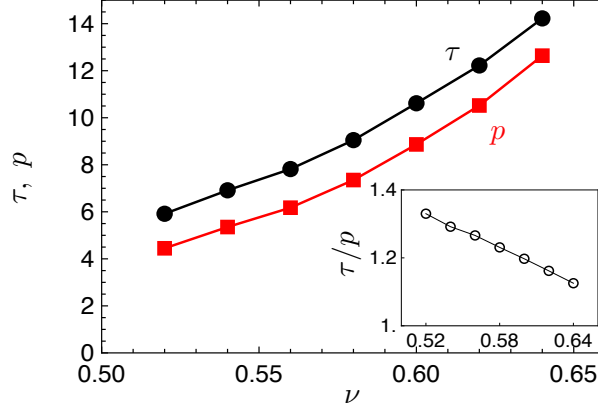
$$\mathbf{F}_R = F_0 \frac{\lambda^{-1} e^{-s/\lambda}}{1 - e^{-s/\lambda}} \mathbf{n}, \quad (4.4)$$

where the range of repulsive force is set by a parameter λ . Because the repulsive force diverges as F_0/s in the limit of contact, $s \rightarrow 0$, some force balance can occur at a finite gap. Thus, the gap s remains positive, and contact forces do not appear in the current system. Note that the divergence in the lubrication coefficient does not guarantee the presence of a minimum $s > 0$, thus it leads to a pathologic singularity in theoretical models (Ball and Melrose 1995).

By solving the force and torque balance equations (4.2) with the hydrodynamic interaction (4.3) and repulsive force (4.4), the linear and angular velocities $(\mathbf{U}, \boldsymbol{\Omega})$ can be determined at each time step. Integrating these velocities \mathbf{U} with a discretized time step, we obtain trajectories of particles. The particle stress tensor \mathbf{T} is given by the symmetrized first moment:

$$\mathbf{T} = \frac{1}{V} \sum_j \frac{\mathbf{r}^{ij} \mathbf{F}^{ij} + \mathbf{r}^{ji} \mathbf{F}^{ji}}{2}, \quad (4.5)$$

with the pairwise forces $\mathbf{F}^{ij} \equiv \mathbf{F}_{\text{Lub}}^{ij} + \mathbf{F}_R^{ij}$ and relative positions $\mathbf{r}^{ij} \equiv \mathbf{r}^i - \mathbf{r}^j$ of all

Figure 2: Shear stress τ and pressure p .

interacting particle pairs. We omit the stress contribution from the fluid. Here, $V = 2aL^2$ is the volume of the monolayer system. Normalizing the symmeterized first moment with the shear stress of the suspending fluid $2\mu\dot{\gamma}$, gives the dimensionless stress $t_{\alpha\beta} \equiv T_{\alpha\beta}/2\mu\dot{\gamma}$. Thus, we have the dimensionless particle pressure $p \equiv -(t_{11} + t_{22})/2$ and the dimensionless particle shear stress $\tau \equiv (t_{11} - t_{22})/2$, respectively.

5. Simulation results

We simulate monolayer systems with 1000 spheres of radius a at area fractions ν between 0.52 and 0.64. We generate initial configurations with a simple algorithm using random numbers. To reduce effects of such artificially generated initial configurations, the post-processing analyses use steady states data from 10 to 50 strain units. The repulsive force is set to be very weak $F_0/\pi a^3 \mu \dot{\gamma} = 10^{-4}$ and short-ranged $\lambda/a = 10^2$.

Fig. 2 shows the area fraction ν dependences of the shear stress τ and pressure p . They increase in a similar manner with ν , but the ratio τ/p decreases gradually. Most of stress is generated by closely approaching particles. We define the near-contacting particles as those with a separation less than one percent of the particle radius. As seen in Fig. 3, more than 90% of shear stress is generated from particle pairs with $0 < s < 0.01$. Moreover, such near-contacting particles generates almost 100% of the pressure p .

We can check the concentration of stress contribution in the very narrow range of s using distribution maps. We calculate the spatial distribution in $\xi \equiv \log s$. The statistics are calculated with discretized bins $\xi_k \equiv \xi_1 + (k-1)\Delta\xi$, $k = 1, \dots, k_{\max}$. $\xi_1 = \log 10^{-7}$ and $\xi_{k_{\max}} = \log 10^{-1}$. The results are plotted with s in a logarithmic scale. Fig. 4(a) displays the probability distribution $P(s, \theta)$ of the same simulation, indicating that particles tend to remain near the stagnation point $(\theta, s) \approx (0, 10^{-6})$. The hot-spot band spreads until $\theta \sim \pi/4$. We also separately calculate the stress of (4.5) constructed with normal forces $\mathbf{F}_n^{ij} \equiv \mathbf{F}^{ij} \cdot \mathbf{n}^{ij} \mathbf{n}^{ij}$ and tangential forces $\mathbf{F}_t^{ij} \equiv \mathbf{F}^{ij} - \mathbf{F}^{ij} \cdot \mathbf{n}^{ij} \mathbf{n}^{ij}$. As shown in Fig. 3(b), 80 % of shear stress τ indeed comes from the normal forces.

Besides systematic motions due to the shearing deformation, particle motions fluctuate due to occasional configurations of surrounding particles. Therefore, it is necessary to reconstruct averaged trajectories to compare with theoretical ones. To this end, we first calculate the averaged relative-velocity field $\langle \mathbf{U}^{(j)} - \mathbf{U}^{(i)} \rangle$ over all interacting pairs i and j in terms of the relative position coordinate $\Delta \mathbf{r}^{ij} = (2a + s, \theta)$. Owing to the symmetry of pure shear, the statistics are taken on a quadrant: $0 < \theta < \pi/2$. Because we consider

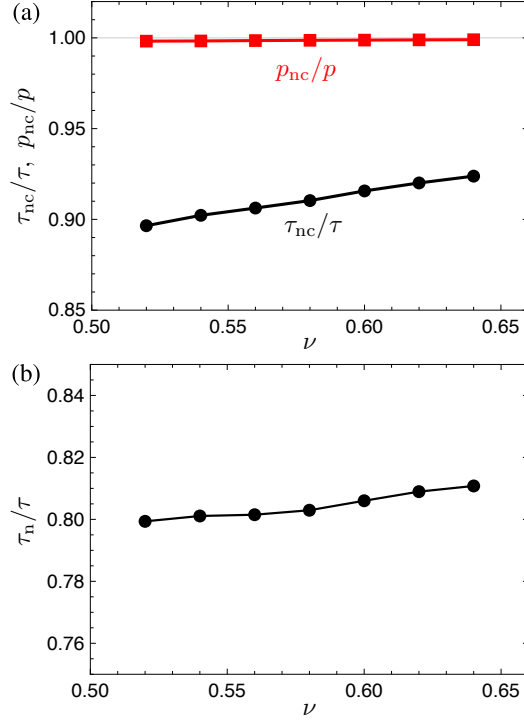


Figure 3: (a) Near-contact contributions to τ and p . (b) Approximately 80 % of the shear stress τ comes from the normal force. The partial stress is obtained using only the normal component of the pairwise force in (4.5).

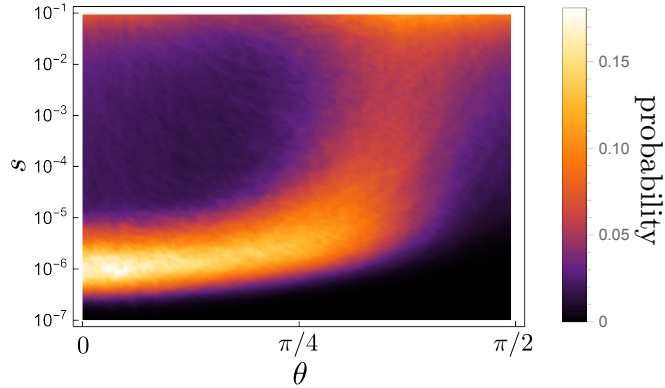


Figure 4: Probability distribution. The s axis is logarithmic.

a situation that is very close to the singularity (Ball and Melrose 1995), the particles tend to approach very close to contact, i.e., a bundle of trajectories is compressed into an extremely narrow range of s . To avoid a loss of precision due to averaging, we carry out the statistical data binning with ξ instead of s .

Once we evaluate the velocity field in the ξ - θ space, i.e., $(\langle \dot{\xi} \rangle = \langle \dot{s}/s \rangle, \langle \dot{\theta} \rangle)$, we can obtain trajectories as streamlines of the velocity field. In Fig. 5 (a) and (b) trajectories of

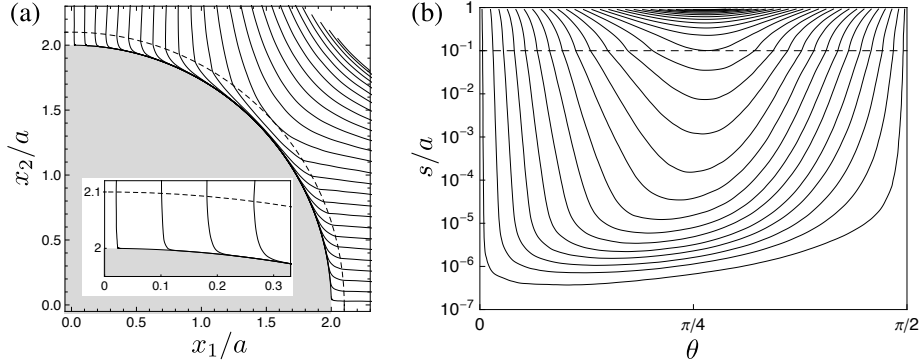


Figure 5: Trajectories reconstructed from the averaged velocity field at $\nu = 0.52$: (a) in the x_1 - x_2 space; (b) in the θ - s space with a logarithmic scale for s . The inset is the zoomed view near x_2 -axis. The hydrodynamic interaction is active only below the dashed line.

the system with $\nu = 0.52$ and initial positions: $(\theta_0, s_0/a) = (q\pi/100, 1)$ ($q = 1, \dots, 25$), are plotted.

6. Model predictions

We take $\bar{s} = 0.02$, $\theta_0 = 10^{-6}$, $s_0 = s_1 = 0.10$, and assume that k varies linearly with ν from 2.0, at $\nu = 0.52$, to 2.5, at $\nu = 0.64$. These values and the relation for k are plausible; but they are influenced by the Stokesian Dynamics simulations. The value \bar{s} gives shear stresses that are close to those measured. The value of θ_0 is the default absolute tolerance of the solver; smaller values of θ_0 have little influence on the shear stress, but do slightly improve the prediction of the pressure. The initial and final values of the separation were those employed in the simulations, and the variation of near-contacting neighbors with area fraction was that measured.

Figure 6 shows the logarithm of the separation along the representative trajectory for $\nu = 0.52$ and $\nu = 0.64$. The representative trajectories have roughly the same shape and extent as the individual trajectories of Fig. 5. Figure 7 shows the logarithm of the distribution of near-contacting neighbors along these trajectories. When evaluated along a representative trajectory, the particle distribution exhibits the same features as the probability distribution of Fig. 4. Figures 6 and 7 indicate the role played by the repulsive force in creating an asymmetry between approach and departure with increases in area fraction, and its influence on the distribution of particles along the trajectory.

In Figs. 8, and 9 we plot the predicted particle shear stress and the predicted particle pressure. The particle pressure exists because of the asymmetry of approach and departure in the trajectory associated with F . Moreover, given Eq. (2.30), we can identify the normal and tangential component of the force, respectively, along $\hat{\mathbf{d}}^{(\text{BA})}$ and $\hat{\mathbf{t}}^{(\text{BA})}$. Then the stress, seen as first moment of the force, can be partitioned in a part contributed by the normal component of the viscous forces and a part contributed by the tangential component of the viscous force. Clearly, particle pressure depends only upon the contribution of the normal forces; less obvious is the fact that the shear stress also depends almost entirely on the contribution to the stress associated with the normal component of the force. This is because the greatest contribution to the stress is where particles have

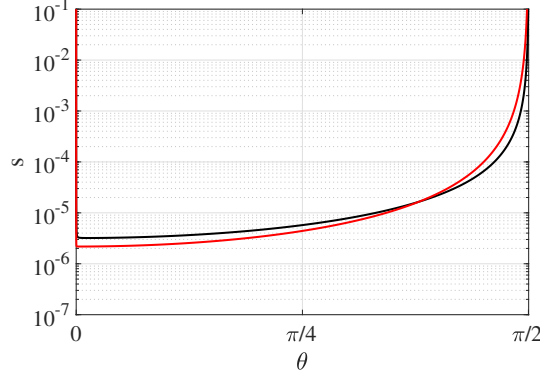


Figure 6: The predicted separation along the representative trajectory, with a logarithmic scale for s , for $\nu = 0.52$, $k = 2.01$ (black) and $\nu = 0.64$, $k = 2.48$ (red), with $\theta_0 = 10^{-6}$, $\hat{F} = 10^{-4}$, and $\bar{s} = 0.02$.

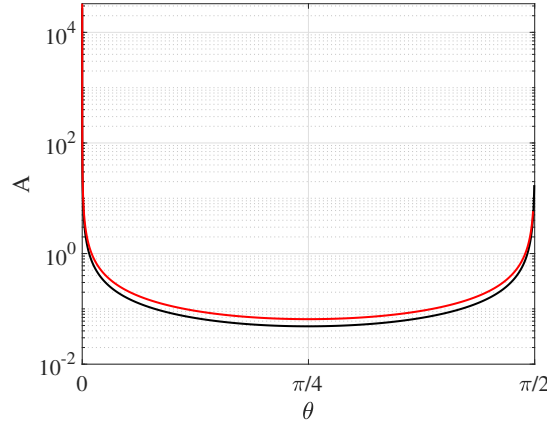


Figure 7: The predicted distribution of near-contacting neighbors along the representative trajectory, with a logarithmic scale for A , for the parameter values of figure 6. For $\nu = 0.52$, $A(\theta_0) = 2.74 \times 10^4$ and $A(\theta_1) = 17.29$; for $\nu = 0.64$, $A(\theta_0) = 3.30 \times 10^4$ and $A(\theta_1) = 5.85$.

the highest concentration, close to $\theta = 0$; here, tangential forces are almost zero and the normal forces are greater.

The predicted particle pressure is somewhat less than that measured in the numerical simulations and the predicted shear stress is somewhat greater. The ratio of shear stress to pressure decreases with area fraction, as in the numerical simulations; but, because of under- and over-predicting, we have a greater value for the ratio. The ratio decreases as the area fraction increases because the asymmetry of the particle distribution about $\pi/4$ increases; the pressure is sensitive to this asymmetry, while the shear stress is not. The information from the Stokesian Dynamics simulation used in the model to obtain a reasonable representation of the measured particle shear stress is, then, also able to generate a particle distribution with the appropriate asymmetry about $\pi/4$ to produce a similar representation of the measured particle pressure.

We next indicate how the structure of the model can be used as the basis for a continuum theory of dense suspensions and to provide a context for existing theories.

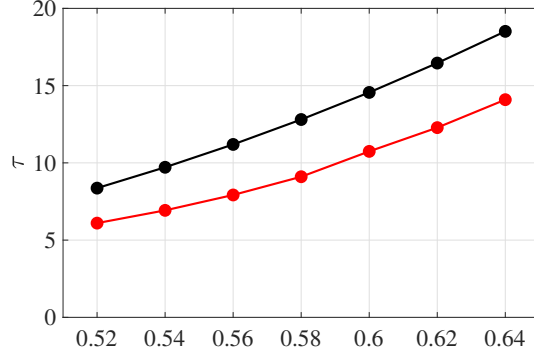


Figure 8: The predicted particle shear stress for different area fractions (black), with $\theta_0 = 10^{-6}$, $F = 10^{-4}$, and $\bar{s} = 0.02$, and that measured in Stokesian Dynamics simulations (red).

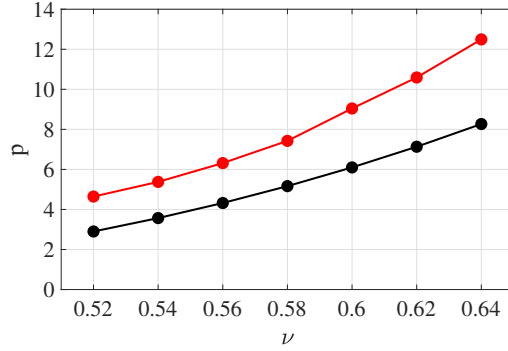


Figure 9: The predicted particle pressure for different area fractions (black) for the parameters of figure 8, and that measured in Stokesian Dynamics simulations (red).

7. Tensorial formulation

As elaborated upon by Onat and Leckie (1988) and Advani and Tucker (1987,1990), the distribution of near-contacting neighbors can be represented by an infinite series with respect to basis functions, such as

$$f_{\alpha\beta} = \hat{d}_\alpha \hat{d}_\beta - \frac{1}{2} \delta_{\alpha\beta} \quad (7.1)$$

and

$$g_{\xi\eta\rho\beta} = \hat{d}_\xi \hat{d}_\eta \hat{d}_\rho \hat{d}_\beta - \frac{1}{6} \left(\delta_{\xi\eta} \hat{d}_\rho \hat{d}_\beta + \hat{d}_\xi \hat{d}_\eta \delta_{\rho\beta} + \hat{d}_\xi \hat{d}_\rho \delta_{\eta\beta} + \hat{d}_\eta \hat{d}_\beta \delta_{\xi\rho} + \delta_{\xi\beta} \hat{d}_\eta \hat{d}_\rho + \hat{d}_\xi \hat{d}_\beta \delta_{\eta\rho} \right) + \frac{1}{24} (\delta_{\xi\eta} \delta_{\rho\beta} + \delta_{\xi\rho} \delta_{\eta\beta} + \delta_{\xi\beta} \delta_{\eta\rho}) : \quad (7.2)$$

$$A(\theta) = \frac{k}{2\pi} (1 + 4\mathcal{Z}_{\alpha\beta} f_{\alpha\beta} + 16\mathcal{B}_{\xi\eta\rho\beta} g_{\xi\eta\rho\beta} + \dots). \quad (7.3)$$

The coefficients \mathcal{Z} and \mathcal{B} are completely traceless and completely symmetric tensors, related to the distribution through

$$\mathcal{Z}_{\alpha\beta} = \int_0^{2\pi} A(\theta) f_{\alpha\beta} d\theta \quad (7.4)$$

and

$$\mathcal{B}_{\xi\eta\rho\beta} = \int_0^{2\pi} A(\theta) g_{\xi\eta\rho\beta} d\theta. \quad (7.5)$$

These are the second and fourth moments of the distribution, respectively.

The stress of Eq.3.1) may be written in terms of these as

$$\begin{aligned} T_{\alpha\beta} = & 4nak \frac{F_0}{\bar{s}} b \delta_{\alpha\beta} - n\pi\mu a^3 (M + N) \mathcal{B}_{\alpha\beta\gamma\eta} D_{\gamma\eta} \\ & - n\pi\mu a^3 (M - N) \frac{k}{4} \delta_{\alpha\eta} \delta_{\beta\gamma} D_{\gamma\eta} \\ & - n\pi\mu a^3 (M + N) \frac{1}{6} \delta_{\alpha\beta} \mathcal{Z}_{\eta\gamma} D_{\gamma\eta} \\ & - n\pi\mu a^3 \frac{2M - N}{6} (\delta_{\alpha\eta} \mathcal{Z}_{\gamma\beta} + \delta_{\beta\eta} \mathcal{Z}_{\gamma\alpha}) D_{\eta\gamma}, \end{aligned} \quad (7.6)$$

where

$$M = \frac{6b}{\bar{s}/a} \quad \text{and} \quad N = 2c_1 + 0.96c_2 - 9.54; \quad (7.7)$$

or, more compactly, as

$$T_{\alpha\beta} = na \left(4kb \frac{F_0}{\bar{s}} \delta_{\alpha\beta} + G_{\alpha\beta\gamma\eta} D_{\gamma\eta} \right), \quad (7.8)$$

where

$$\begin{aligned} G_{\alpha\beta\gamma\eta} = & -n\pi\mu a^3 \left[\frac{M - N}{4} k \delta_{\alpha\eta} \delta_{\beta\gamma} + \frac{M + N}{6} \delta_{\alpha\beta} \mathcal{Z}_{\eta\gamma} + \frac{2M - N}{6} (\delta_{\alpha\eta} \mathcal{Z}_{\gamma\beta} + \delta_{\beta\eta} \mathcal{Z}_{\gamma\alpha}) \right] \\ & - n\pi\mu a^3 (M + N) \mathcal{B}_{\alpha\beta\gamma\eta}. \end{aligned} \quad (7.9)$$

The stress depends only on the second and fourth moments of the distribution, although an approximation of the distribution in terms of these does not provide a good representation of it. With knowledge of the distribution function, it is possible to evaluate the components of the second and fourth moments. In particular, when $F = 0$, the only non-zero components are $\mathcal{B}_{1111} = \mathcal{B}_{2222} = -\mathcal{B}_{1122}$; when $F \neq 0$, then $\mathcal{Z}_{11} = -\mathcal{Z}_{22}$ are also different from zero. For example, when $\nu = 0.64$, $k = 2.50$ and $\hat{F} = 10^{-4}$, their numerical values are $\mathcal{B}_{1111} = 0.25$ and $\mathcal{Z}_{11} = -0.57$. Then, with Eq. (7.8), the dimensionless particle pressure is

$$p = -\nu \frac{b}{\bar{s}} (F - 3\mathcal{Z}_{11}) = 8.51 \quad (7.10)$$

With the equilibrium equations, it is possible to characterize the role played by moment equilibrium in determining features of the trajectory and the distribution of particles along it. Ignoring moment equilibrium is equivalent to taking $S = 0$, or $c_2 = 0$ in Eq. (2.27). This has an important influence on $\dot{\theta}$. Then, because both the distribution of near-contacting neighbors and the interval over which it is defined depend upon $\dot{\theta}$, there is a dependence of the stress upon it. For example, when $\nu = 0.64$ and moment equilibrium is ignored, p is 14.81, rather than 8.51. That is, the value of p is affected by moment equilibrium through the distribution. In contrast, τ is 18.60, rather than 18.94 and changes little because it is independent of the shape of the distribution.

In the absence of the knowledge of the distribution function, it is possible to develop evolution equations for the approximate determination of its moments (e.g., Prantil et al., 1993). Phan-Thien (1995) and Stickel et al. (2006) employ such an equation for the second moment, and break the symmetry of approach and departure by including a term

in it that is proportional to $[\text{tr}(\mathbf{D}^2)/2]^{1/2}$. Goddard (2006) introduces a memory integral for the second moment - a representation for the solution to its evolution equation - that breaks this symmetry by incorporating a term proportional to the \mathbf{D}^2 . Theories of this type produce stress relations that are linear in the strain rate; that is, rate-dependent. In contrast, we employ only a short-range repulsive force that is independent of the shear rate. Consequently, our stress relation contains contributions that are independent of rate.

8. Conclusion

We have considered a plane, pure shearing flow of a dense layer of spheres in a viscous fluid. In addition to the viscous forces associated with the flow, we assumed that there was a short-range repulsive force between the spheres. We focused on pairs of spheres, assumed that their neighbors translate with the average flow, and required that they be in force and moment equilibrium with each other and their neighbors. We then assumed that the neighborhoods of pairs with the same orientation were equal to the average over that orientation; this permitted us to write equations for the radial and angular velocity of the relative motion of a single pair as they began and ended an interaction, and the orientation of their line of centers with the axis of greatest compression of the flow.

The possible determination of the distribution of particles along the trajectory then leads to expressions for the particle shear stress and pressure. Stokesian Dynamics simulations provided a value of particle shear stress that permitted the determination of a starting angle for the trajectories and the separation of near-contacting neighbors. The variation of the shear stress with area fraction suggested the variation of the number of near-contacting neighbors per particle with area fraction. With this information, numerical values of the particle distribution and the particle pressure could be calculated.

The simplicity of the micro-mechanical model makes it possible to understand the influence of the normal and tangential components of the viscous force and the short-range repulsive force on the shape of the trajectory and the distribution of particles along it. It also permits the derivation of a continuum theory for dense suspensions based on the micro-mechanics of equilibrated pairs of particles and a better understanding of those based on phenomenology.

9. Appendix A

Force equilibrium equation for particle A is

$$\begin{aligned}
0 = & 6\pi\mu a K_{\alpha\beta}^{(BA)} v_{\beta}^{(BA)} - \frac{F_0}{s^{(BA)}} \hat{d}_{\alpha}^{(BA)} - 9.54\pi\mu a^2 \left(\hat{t}_{\beta} D_{\beta\xi} \hat{d}_{\xi} \right) \hat{t}_{\alpha}^{(BA)} + \pi\mu a^2 \left[\ln \left(\frac{a}{s^{(BA)}} \right) - 0.96 \right] \omega^{(A)} \hat{t}_{\alpha}^{(BA)} \\
& + \pi\mu a^2 \ln \left(\frac{a}{s^{(BA)}} \right) \omega^{(B)} \hat{t}_{\alpha}^{(BA)} + \sum_{n \neq B}^{N^{(A)}} \left\{ \frac{3}{s} a^2 \pi \mu \left(D_{\beta\xi} \hat{d}_{\xi}^{(nA)} \hat{d}_{\beta}^{(nA)} \right) \hat{d}_{\alpha}^{(nA)} + \pi\mu a^2 \left[\ln \left(\frac{a}{s} \right) - 0.96 \right] \omega^{(A)} \hat{t}_{\alpha}^{(nA)} \right\} \\
& + \sum_{n \neq B}^{N^{(A)}} \left\{ 2a^2 \pi \mu \left[\ln \left(\frac{a}{s} \right) - 0.96 \right] \left(D_{\beta\xi} \hat{t}_{\xi}^{(nA)} \hat{d}_{\beta}^{(nA)} \right) \hat{t}_{\alpha}^{(nA)} - \frac{F_0}{s} \hat{d}_{\alpha}^{(nA)} \right\}. \tag{9.1}
\end{aligned}$$

Similar expression can be written for particle B . The difference between force equilibrium A and B leads to

$$\begin{aligned}
 0 = & 12\pi\mu a K_{\alpha\beta}^{(BA)} v_{\beta}^{(BA)} - 2 \frac{F_0}{s^{(BA)}} \hat{d}_{\alpha}^{(BA)} - 2 \times 9.54\pi\mu a^2 \left(\hat{t}_{\beta}^{(BA)} D_{\beta\xi} \hat{d}_{\xi}^{(BA)} \right) \hat{t}_{\alpha}^{(BA)} \\
 & + a^2 \pi\mu \left[2 \ln \left(\frac{a}{s^{(BA)}} \right) - 0.96 \right] S \hat{t}_{\alpha}^{(BA)} + a^2 \pi\mu \left[\ln \left(\frac{a}{s} \right) - 0.96 \right] S \varepsilon_{\alpha\beta} Y_{\beta}^{(BA)} \\
 & + 2 \frac{3}{s} a^2 \pi\mu D_{\beta\xi} J_{\alpha\xi\beta}^{(BA)} + 2a^2 \pi\mu \left[2 \ln \left(\frac{a}{s} \right) - 1.92 \right] D_{\beta\xi} J_{\alpha\xi\beta}^{(BA)} - 2 \frac{F_0}{s} Y_{\alpha}^{(BA)},
 \end{aligned}$$

where

$$S = \omega^{(A)} + \omega^{(B)},$$

$$J_{\alpha\xi\beta}^{(BA)} = \sum_{n \neq B}^{N^{(A)}} \hat{d}_{\alpha}^{(nA)} \hat{d}_{\beta}^{(nA)} \hat{d}_{\xi}^{(nA)},$$

and

$$Y_{\alpha}^{(BA)} = \sum_{n \neq B}^{N^{(A)}} \hat{d}_{\alpha}^{(nA)}.$$

Moment equilibrium for particle A is

$$\begin{aligned}
 0 = & 6\pi\mu a K_{\alpha\beta}^{(BA)} v_{\beta}^{(BA)} \varepsilon_{\alpha\rho} \hat{d}_{\rho}^{(BA)} - 9.54\pi\mu a^2 \left(\hat{t}_{\beta} D_{\beta\xi} \hat{d}_{\xi} \right) + \pi\mu a^2 \left[\ln \left(\frac{a}{s^{(BA)}} \right) - 0.96 \right] \omega^{(A)} \\
 & + \pi\mu a^2 \ln \left(\frac{a}{s^{(BA)}} \right) \omega^{(B)} + \varepsilon_{\alpha\rho} \sum_{n \neq B}^{N^{(A)}} \left\{ \frac{3}{s} a^2 \pi\mu \left(D_{\beta\xi} \hat{d}_{\xi}^{(nA)} \hat{d}_{\beta}^{(nA)} \right) \hat{d}_{\alpha}^{(nA)} + \pi\mu a^2 \left[\ln \left(\frac{a}{s} \right) - 0.96 \right] \omega^{(A)} \hat{t}_{\alpha}^{(nA)} \right\} \hat{d}_{\rho}^{(nA)} \\
 & + \varepsilon_{\alpha\rho} \sum_{n \neq B}^{N^{(A)}} \left\{ 2a^2 \pi\mu \left[\ln \left(\frac{a}{s} \right) - 0.96 \right] \left(D_{\beta\xi} \hat{t}_{\xi}^{(nA)} \hat{d}_{\beta}^{(nA)} \right) \hat{t}_{\alpha}^{(nA)} - \frac{F_0}{s} \hat{d}_{\alpha}^{(nA)} \right\} \hat{d}_{\rho}^{(nA)}. \tag{9.2}
 \end{aligned}$$

A similar expression holds for particle B. The sum of moment equilibrium for particles A and B is

$$\begin{aligned}
 0 = & 12\varepsilon_{\alpha\beta} K_{\alpha\mu}^{(BA)} v_{\mu}^{(BA)} \hat{d}_{\beta}^{(BA)} - 2 \times 9.54a \left(\hat{t}_{\mu}^{(BA)} D_{\mu\xi} \hat{d}_{\xi}^{(BA)} \right) \\
 & + a \left[2 \ln \left(\frac{a}{s^{(BA)}} \right) - 0.96 \right] S + a \left[\ln \left(\frac{a}{s} \right) - 0.96 \right] S (k-1) \\
 & + 2a \left[2 \ln \left(\frac{a}{s} \right) - 1.92 \right] \varepsilon_{\xi\nu} A_{\nu\mu}^{(BA)} D_{\mu\xi}, \tag{9.3}
 \end{aligned}$$

where

$$A_{\nu\mu}^{(BA)} = \sum_{n \neq B}^{N^{(A)}} \hat{d}_{\mu}^{(nA)} \hat{d}_{\nu}^{(nA)}.$$

In both the difference of force equilibrium and the sum of moment equilibrium, we have made the following approximations

$$A_{\nu\mu}^{(BA)} = A_{\nu\mu}^{(AB)},$$

$$J_{\alpha\xi\beta}^{(BA)} = -J_{\alpha\xi\beta}^{(AB)},$$

and

$$Y_{\alpha}^{(BA)} = -Y_{\alpha}^{(AB)}.$$

The projection of the difference in force equilibrium along the direction orthogonal to $t_\alpha^{(BA)}$ is

$$3\pi\mu a \frac{a}{s^{(BA)}} \dot{s}^{(BA)} - 2 \frac{F_0}{s^{(BA)}} + 6\pi\mu a^2 \frac{a}{\bar{s}} \hat{d}_\alpha J_{\alpha\beta\gamma} D_{\beta\gamma} - 2 \frac{F_0}{\bar{s}} Y_\alpha \hat{d}_\alpha = 0, \quad (9.4)$$

while the component along $t_\alpha^{(BA)}$ is

$$\begin{aligned} 0 = & 12\pi\mu a K_{\alpha\beta}^{(BA)} v_\beta^{(BA)} t_\alpha^{(BA)} - 2 \times 9.54\pi\mu a^2 \left(\hat{t}_\beta^{(BA)} D_{\beta\xi} \hat{d}_\xi^{(BA)} \right) \\ & + a^2 \pi\mu \left[2 \ln \left(\frac{a}{s^{(BA)}} \right) - 0.96 \right] S + a^2 \pi\mu \left[\ln \left(\frac{a}{\bar{s}} \right) - 0.96 \right] S \varepsilon_{\alpha\beta} Y_\beta^{(BA)} t_\alpha^{(BA)} \\ & + 2 \frac{3}{\bar{s}} a^2 \pi\mu D_{\beta\xi} J_{\alpha\xi\beta}^{(BA)} t_\alpha^{(BA)} + 2a^2 \pi\mu \left[2 \ln \left(\frac{a}{\bar{s}} \right) - 1.92 \right] D_{\beta\xi} J_{\alpha\xi\beta}^{(BA)} t_\alpha^{(BA)}. \end{aligned} \quad (9.5)$$

Using Eq. (9.5) and Eq. (9.3), we solve for S :

$$S = - \frac{12b}{(4b - k + 1) \bar{s} [\ln(1/\bar{s}) - 0.96]} \sin 2\theta,$$

or

$$S = -2c_2 \sin 2\theta, \quad (9.6)$$

where

$$c_2 = \frac{6b / [\bar{s} (4b - k + 1)]}{\ln(1/\bar{s}) - 0.96}.$$

10. Appendix B

The Matlab m-files for the numerical solution of the ordinary differential equations and boundary conditions follow.

```

function dydx = ODE(x,y,parameters,k,F,sbar,theta0)

% y(1)=s, y(2)=A, y(3)=Int(A)
% k average number of contacts per particle; nu area fraction;
% F strength of repulsion, sbar average separation
% Interval: x from 0 to 1, theta1 is the parameter
% sol = bvp4c(@ODE,@BC,sol0,[],2.0,1e-4,0.02,1e-8)

alpha = -3*sqrt(3)*(k-1)/(16*pi);

theta1 = parameters(1,1);

deltheta = theta1-theta0;
theta = theta0+deltheta*x;

s = y(1);

c1 = 4.77-3*alpha/sbar;
c2 = 6*alpha/(sbar*(4*alpha-k+1))*1/(log(1/sbar)-0.96);

sdot = 2/3*F*(1+4*alpha*s/sbar)+2*alpha*s/sbar*2*cos(2*theta);
thetadot = (c1+c2*log(1/s))*sin(2*theta)/(log(1/s)+3.84);

ptdtdth = 2*thetadot*cot(2*theta);
ptdotds = 1/(log(1/s)+3.84)*(1/s)*(thetadot-c2*sin(2*theta));
dtdtdth = ptdtdth+ptdotds*sdot/thetadot;

dsdth = sdot/thetadot;
dAdth = -y(2)*dtdtdth/thetadot;

dydx=[
    deltheta*dsdth % s
    deltheta*dAdth % A
    deltheta*y(2) % Int(A)
];

function res = BC(ya,yb,parameters,k,F,sav,theta0)

% y(1)=s, y(2)=A, y(3)=Int(A)

theta1 = parameters(1,1);

res=[
    ya(1)-0.1 % sp(0)
    yb(1)-0.1 % sp(1)
    ya(3) % Int Ap
    yb(3)-k/4 % Int Ap
];

```

This research was partially supported by the National Science Foundation under Grant No. NSF PHY-1748958 and by the Gruppo Nazionale della Fisica Matematica (Italy). R. S. acknowledges the support from the Wenzhou Institute, UCAS.

11. Declaration of Interests

The authors report no conflict of interest.

REFERENCES

- Advani, S. G. & Tucker, C. L. 1987 The Use of Tensors to Describe and Predict Fiber Orientation in Short Fiber Composites. *J. Rheol.* **31**, 751–784.
- Advani, S.G. & Tucker, C.L. 1990 Closure approximations for three dimensional structure tensors. *J. Rheol.* **34**, 367–386.
- Ball, R. C. & Melrose, J. R. 1995 Lubrication breakdown in hydrodynamic simulations of concentrated colloids. *Adv. Colloid Interface Sci.* **59**, 19–30.
- Boyer, F., Guazzelli, E. & Pouliquen, O. 2011 Unifying Suspension and Granular Rheology. *Phys. Rev. Lett.* **107**, 188301.
- Brady, J. F. & Bossis, G. 1988 Stokesian dynamics. *Annu. Rev. Fluid Mech.* **20**(1), 111–157.
- Goddard, J. D. 2006 A dissipative anisotropic fluid model for non-colloidal particle suspensions. *J. Fluid Mech.* **568**, 1–17.
- Guazzelli, E. & Pouliquen, O. 2018 Rheology of dense granular suspensions. *J. Fluid Mech.* **852**, P1:1–73.
- Jeffrey, D. J. 1992 The calculation of low reynolds number resistance functions for two unequal spheres. *Phys. Fluids A* **4**, 16–29.
- Jeffrey, D. J. & Onishi, Y. 1984 Calculation of the resistance and mobility functions for two unequal rigid spheres in low-Reynolds-number flow. *J. Fluid Mech.* **139**, 261–290.
- Jenkins, J. T., La Ragione, L., Johnson, D. & Makse, H. A. 2005 Fluctuations and effective moduli of an isotropic, random aggregate of identical, frictionless spheres. *J. Mech. Phys. of Sol.* **53**, 197–225.
- Jenkins, J. T. & La Ragione, L. 2015 An analytical determination of microstructure and stresses in a dense, sheared monolayer of non-Brownian spheres. *J. Fluid Mech.* **763**, 218–236.
- Kraynik, A. M. & Reinelt, D. A. 1992 Extensional motions of spatially periodic lattices. *Int. J. Multiphase Flow* **18**, 1045–1059.
- Love, A. E. H. 1944 A Treatise on the Mathematical Theory of Elasticity, Third Edition. Cambridge University Press, Cambridge.
- Mari, R., Seto, R., Morris, J. F. & Denn, M. M. 2014 Shear thickening, frictionless and frictional rheologies in non-Brownian suspensions. *J. Rheol.* **58**, 1693–1724.
- Nazockdast, E. & Morris, J. F. 2012a Microstructural theory and rheology of concentrated suspensions. *J. Fluid Mech.* **713**, 420–452.
- Nazockdast, E. & Morris, J. F. 2012b Effect of repulsive interaction on structure and rheology of sheared colloidal suspensions. *Soft Matter* **8**, 4223–4234.
- Nazockdast, E. & Morris, J. F. 2013 Pair-particle dynamics and microstructure in sheared colloidal suspensions: Simulation and Smoluchowski theory. *Phys. Fluids* **25**, 25070601.
- Nott, P. R. & Brady, J. F. 1994 Pressure-driven flow of suspensions: simulation and theory. *J. Fluid Mech.* **275**, 157–199.
- Onat, E. T. & Leckie, F. A. 1988 Representation of Mechanical Behavior in the Presence of Changing Internal Structure. *J. Appl. Mech.* **55**, 1–10.
- Phan-Thien, N. 1995 Constitutive relation for concentrated suspensions in Newtonian liquids. *J. Rheol.* **39**, 679–695.
- Prantil, V. C., Jenkins, J. T. & Dawson, P. R. 1993 An analysis of texture and plastic spin for planar polycrystal. *J. Mech. Phys. of Sol.* **41**, 1357–1382.
- Seto, R., Giusteri & Martiniello, A. 2017 Microstructure and thickening of dense suspensions under extensional and shear flows. *J. Fluid Mech.* **825**, R3.
- Seto, R., Mari, R., Morris, J. F. & Denn, M. M. 2013 Discontinuous shear thickening of frictional hard-sphere suspensions *Phys. Rev. Lett.* **111**, 218301

- Sierou, A. & Brady, J. F. 2002 Rheology and microstructure in concentrated noncolloidal suspensions. *J. Rheol.* **46**, 1031–1056.
- Singh, A. & Nott, P. R. 2000 Normal stresses and microstructure in bounded sheared suspensions via Stokesian Dynamics simulations. *J. Fluid Mech.* **412**, 279–301.
- Stickel, J. J., R. J. Phillips & Powell, R. L. 2006 A constitutive model for microstructure and total stress in particulate suspensions. *J. Rheol.* **50**, 379–413.
- Thomas, J. E., Ramola, K., Singh, A., Mari, R., Morris, J. F. & Chakraborty, B. 2018 Microscopic origin of frictional rheology in dense suspensions: correlations in force space. *Phys. Rev. Letts.* **121**, 128002.
- Todd, B. D. & Daivis, P. J. 1998 Nonequilibrium Molecular Dynamics Simulations of Planar Elongational Flow with Spatially and Temporally Periodic Boundary Conditions *Phys. Rev. Lett.* **81**, 1118–1121
- Torquato, S. 1995 Nearest-neighbor statistics for packings of hard spheres and disks. *Phys. Rev E* **51**, 3170–3184.